The Astrophysical Journal, 952:16 (7pp), 2023 July 20 https://doi.org/10.3847/1538-4357/acdb66

# Magnetic Helicity Associated with the Proton Temperature Anisotropy Instabilities in the Presence of an Imbalanced Solar Wind Turbulence

S. A. Markovskii and Bernard J. Vasquez

Space Science Center, University of New Hampshire, Durham, NH 03824, USA; sergei.markovskii@unh.edu, bernie.vasquez@unh.edu

*Received 2022 November 30; revised 2023 May 3; accepted 2023 June 3; published 2023 July 14*

## Abstract

Some of the most common processes in the solar wind, such as turbulence and wave generation by instabilities, are associated with spectral magnetic helicity. Therefore, the helicity is a convenient tool to investigate these processes. We use three-dimensional nonlinear kinetic simulations with particle ions and fluid electrons to analyze the magnetic helicity produced by proton temperature anisotropy instabilities coexisting with an ambient turbulence. The symmetry of the unstable system is violated by alpha-particle streaming with respect to protons along the mean magnetic field. At the same time, the turbulent fluctuations are also imbalanced by a nonzero cross-helicity. We show that in the nonlinear phase of the instability the resulting helicity structure is different from the prediction of the linear theory. In particular, it contains sign reversals and multiple domains of nonzero helicity. The turbulence generates its own magnetic helicity signature, which extends over a wide range of angles around the direction perpendicular to the mean magnetic field, and can have a sign the same as or opposite to that of the instability. These findings are consistent with the observed helicity spectra in the solar wind.

*Unified Astronomy Thesaurus concepts:* Space plasmas (1544); Interplanetary turbulence (830); Solar wind (1534)

## 1. Introduction

The spectral magnetic helicity is an important characteristic of the solar wind fluctuations. It is associated with some of the most common processes in the solar wind, such as turbulence and wave generation by thermal ion instabilities. Since it is affected by the fluctuation properties, it can be used to analyze the physical processes responsible for the fluctuations (e.g., He et al. 2012, 2015; Bowen et al. 2020a, 2020b; Huang et al. 2020; Zhao et al. 2021).

The spectral helicity was first discussed in connection with the turbulence by Matthaeus et al. (1982). They measured a two-point spatial correlation function of the magnetic field in the solar wind and demonstrated that it is sufficient to derive the helicity under the assumption that the turbulence is spatially homogeneous. It was later shown by Goldstein et al. (1994) that there is a helicity signature at the ion kinetic scales, i.e., nonzero values confined to a certain spectral range.

The turbulence studies initially used a global mean magnetic field calculated from the whole solar wind interval that determines the spectrum. Alternatively, one can consider a local mean magnetic field at the scale of the sampled fluctuation. He et al. (2011) and Podesta & Gary (2011a) evaluated the magnetic helicity based on the local mean approach, in which the direction of the mean magnetic field was calculated as a function of scale and time. They found that helicity structure is, in fact, more complex with multiple signatures of both senses of handedness at oblique and nearly parallel wavevectors to the mean magnetic field.

The oblique fluctuations may be interpreted as a strong imbalanced turbulence. In particular, as shown by Markovskii & Vasquez (2013, 2016), a strictly two-dimensional (2D) turbulent cascade perpendicular to the mean magnetic field results in a magnetic helicity signature at small, ion kinetic scales if the cross-helicity at large, inertial-range scales is not zero. This is true despite the fact that no linear waves are propagating along the mean field in this configuration. The strong-turbulence interpretation is consistent with the observational data because its helicity signature has a finite extent in the wavenumber space.

The nearly parallel fluctuations were assumed to be unstable waves generated by the proton temperature anisotropy. Based on the linear theory of the instability, Podesta & Gary (2011b) have demonstrated that the growth rates of the waves propagating in the direction of the magnetic field and the opposite direction may be unequal. This happens when the symmetry of the system is broken, for instance, by a relative drift of one ion species with respect to another. Therefore, at least at the initial phase of the wave growth, the imbalance of the circularly polarized waves produces a nonzero magnetic helicity.

The linear theory of the instabilities provides a guidance, but the intensities of the waves in the saturated state are not necessarily what it predicts. The reason is that the driving distribution function evolves as the instability grows. In the case of the perpendicular higher than parallel proton temperature, the relative intensity of the waves propagating in the opposite directions in the nonlinear phase depends on the wavenumber (Markovskii et al. 2018). As a consequence, the magnetic helicity signature of the instability contains a sign reversal instead of having a uniform sign throughout its wavenumber range.

There is another consequence of the nonlinearity. The unstable modes that did not contribute to the helicity at earlier times may do so at later times. When the perpendicular proton temperature is larger than the parallel one, the oblique mirror mode initially grows slower than the nearly parallel proton-cyclotron mode but eventually comes to dominate the spectrum (Markovskii et al. 2018). However, the mirror mode has zero helicity and does not contribute to the overall signature. In the

**Table 1**
Parameters of the Simulation Runs

| Run | $D$[a] | $N_{\parallel}$ | $N_{\perp}$ | $\sigma_c$[b] | ppc[c] | $\alpha$pc[d] | $n_{0\alpha}/n_{0p}$ | $V_{d\,\alpha}/V_{\rm A}$ | $\beta_{\parallel p}$ | $T_{\perp p}/T_{\parallel p}$ |
|---|---|---|---|---|---|---|---|---|---|---|
| I | 3 | 256 | 128 | N/A | 1000 | 500 | 0.1 | 0.245 | 1.06 | 2.24 |
| II | 3 | 256 | 128 | N/A | 1500 | 500 | 0.05 | 0.5 | 2.5 | 0.4 |
| III | 3 | 256 | 128 | −0.8 | 1500 | 500 | 0.05 | 0.508 | 2.56 | 0.38 |
| IV | 2 | N/A | 512 | −0.8 | 6000 | 3000 | 0.1 | 0.25 | 1.0 | 2.4 |
| V | 2 | N/A | 512 | −0.8 | 9000 | 3000 | 0.05 | 0.508 | 2.56 | 0.38 |
| VI | 3 | 256 | 128 | 0.8 | 1500 | 500 | 0.05 | −0.508 | 2.56 | 0.38 |

**Notes.**
[a] $D$ is the run dimensionality.
[b] The initial background in runs I and II is uniform with no turbulence. Therefore, no cross-helicity is specified.
[c] Protons per cell.
[d] Alpha particles per cell.

present paper, we investigate the opposite sense of the proton temperature anisotropy leading to the fire-hose instability. This situation is somewhat similar because, over time, the oblique fire-hose mode overtakes the parallel mode (Hellinger & Matsumoto 2001; Hellinger & Trávníček 2006). The difference is that the oblique fire hose can be associated with a nonzero helicity in the nonlinear phase.

We carry out numerical simulations including the nonlinear effects. The covered spatial scales range from the fluid to the ion kinetic limit. The simulations involve both an imbalanced ambient turbulence with a nonzero cross-helicity and instabilities whose symmetry is violated by a relative streaming of the alpha particles with respect to the protons. When the instabilities develop in a turbulent background, their properties can change (Markovskii et al. 2019, 2020; Markovskii & Vasquez 2022a, 2022b). Therefore, the turbulence has to be taken into account when it coexists with the instability for an accurate description of the helicity signature.

## 2. Numerical Setup

We perform 2D and three-dimensional (3D) hybrid simulations with particle-in-cell protons and a quasi-neutralizing electron fluid. The numerical code is described by Terasawa et al. (1986) and Vasquez (1995, 2015). The code solves the following equations:

$$\frac{d\boldsymbol{x}_{p,\alpha}}{dt} = \boldsymbol{v}_{p,\alpha}, \tag{1}$$

$$m_{p,\alpha}\frac{d\boldsymbol{v}_{p,\alpha}}{dt} = q_{p,\alpha}\left(\boldsymbol{E} + \frac{1}{c}[\boldsymbol{v}_{p,\alpha}\times\boldsymbol{B}]\right), \tag{2}$$

$$\frac{1}{c}\frac{\partial\boldsymbol{B}}{\partial t} = -\nabla\times\boldsymbol{E}, \tag{3}$$

$$\boldsymbol{E} = \frac{1}{c}[\boldsymbol{B}\times\boldsymbol{V}_e], \tag{4}$$

$$\nabla\times\boldsymbol{B} = \frac{4\pi e}{c}(n_p\boldsymbol{V}_p + 2n_\alpha\boldsymbol{V}_\alpha - n_e\boldsymbol{V}_e), \tag{5}$$

where $n_e = n_p + 2n_\alpha$. The quantities $\boldsymbol{x}_{p,\alpha}$ and $\boldsymbol{v}_{p,\alpha}$ are positions and velocities of individual protons and alpha particles, $q_{p,\alpha}$ is the ion charge, $\boldsymbol{E}$ is the electric field, $c$ is the speed of light, $e$ is the elementary charge, $n_e$ is the electron number density, and $\boldsymbol{V}_e$ is the electron fluid velocity. The proton and alpha number density $n_{p,\alpha}$ and bulk velocity $\boldsymbol{V}_{p,\alpha}$ for each spatial cell are calculated as moments of the distribution. The mean magnetic field $\boldsymbol{B}_0$ is in the positive $x$-direction.

The electron temperature is set to zero, and the electron fluid is massless. The simulation box sizes are $L_\perp = 64$ in the $y$- and $z$-directions and $L_\parallel = 256$ in the $x$-direction in units of the proton inertial length $V_{\rm A}\Omega_p^{-1}$. The numbers of cells in the simulation grid in the parallel $x$-direction $N_\parallel$ and in the perpendicular $y$- and $z$-directions $N_\perp$ vary from run to run and are given in Table 1. The time step is 0.01 in units of the inverse proton gyrofrequency $\Omega_p^{-1}$. Here $\Omega_p$ and the Alfvén speed $V_{\rm A}$, and thereby the spatial and temporal scales, are defined with the initial mean values of the magnetic field $B_0$ and the proton number density $n_{0p}$. The boundary conditions are periodic.

In the runs where the instability develops in a turbulent environment, we initiate the turbulent cascade as follows. The magnetic field fluctuations $\Delta\boldsymbol{B}(t, \boldsymbol{x})$ at $t = 0$ are given by the formula

$$\Delta\boldsymbol{B}(0, \boldsymbol{x}) = \frac{1}{2}\sum_{\boldsymbol{k}}[\delta\boldsymbol{B}(0, \boldsymbol{k})\exp(i(\boldsymbol{k}\cdot\boldsymbol{x} + \phi(\boldsymbol{k}))) + \text{c.c.}], \tag{6}$$

where $\boldsymbol{x}$ is the Cartesian spatial position vector, $\boldsymbol{k}$ is the wavevector, and $\phi(\boldsymbol{k})$ is a random phase. The relative total rms amplitude of the magnetic field fluctuations is set to

$$A \equiv \left[\frac{1}{N_\parallel\times N_\perp^2}\sum_{\boldsymbol{x}}\frac{|\Delta\boldsymbol{B}(0, \boldsymbol{x})|^2}{B_0^2}\right]^{1/2} = 0.15. \tag{7}$$

The proton and alpha bulk velocity fluctuations $\Delta\boldsymbol{V}_{p,\alpha}$ are defined in the same way as $\Delta\boldsymbol{B}$ in Equation (6). The components of the vectors $\delta\boldsymbol{B}(0, \boldsymbol{k})$ and $\delta\boldsymbol{V}_{p,\alpha}(0, \boldsymbol{k})$ obey the polarization relations of linear Alfvén waves in the cold multifluid MHD limit. This is merely a convenient way to control the initial cross-helicity and produce strong nonlinear interactions to quickly develop the turbulent cascade. It does not mean that such waves exist in our configuration, and they are not meant to be self-consistent solutions of Equations (1)–(5).

The initial seed spectrum consists of eight modes divided into two groups. Their wavevectors $(k_x, k_y, k_z)$ are $(0, 0, k_0)$, $(0, k_0, k_0)$, $(0, k_0, 0)$, $(0, k_0, -k_0)$ and $(0, 0, -k_0)$, $(0, -k_0, -k_0)$, $(0, -k_0, k_0)$, $(0, -k_0, k_0)$, where $k_0 = 2\pi/L_\perp$. The groups are assigned two different amplitudes, with the amplitudes of the modes in each group being the same. By adjusting the difference between these amplitudes, we achieve a desired nonzero cross-helicity. We take the net fluctuating normalized cross-helicity of the system in the form

$$\sigma_c = 2\sum_{x,y,z} \frac{\Delta \boldsymbol{V} \cdot \Delta \boldsymbol{B}}{V_{\rm A}\, B_0} \Bigg/ \sum_{x,y,z} \left( \frac{|\Delta \boldsymbol{V}|^2}{V_{\rm A}^2} + \frac{|\Delta \boldsymbol{B}|^2}{B_0^2} \right), \qquad (8)$$

where $\Delta \boldsymbol{V}$ is the fluctuation of the bulk velocity of the plasma as a whole. The initial values of $\sigma_c$ in the simulation runs are given in Table 1. The imbalance introduced by the nonzero cross-helicity produces a nonzero magnetic helicity of the turbulence when it develops at later times.

The ion distribution functions are loaded as drifting bi-Maxwellians

$$f_{p,\alpha} = \frac{n_{0p,\alpha}}{\pi^{3/2} V_{T\parallel p,\alpha} V_{T\perp p,\alpha}^2} \exp \times \left( -\frac{(v_x - V_{d\,p,\alpha} - \Delta V_{x\,p,\alpha})^2}{V_{T\parallel p,\alpha}^2} - \frac{|\boldsymbol{v}_\perp - \Delta \boldsymbol{V}_{\perp p,\alpha}|^2}{V_{T\perp p,\alpha}^2} \right), \qquad (9)$$

where $V_T = \sqrt{2k_{\rm B}T/m}$ is the ion thermal speed, $k_{\rm B}$ is the Boltzmann constant, $T = (T_\parallel + 2T_\perp)/3$ is the total ion temperature, and the subscripts "$\parallel$" and "$\perp$" refer to the direction of the background magnetic field. The drift speed of the protons $V_{d\,p} = 0$. The initial ion number densities and temperatures are spatially uniform. The alpha-particle temperature is isotropic, and $T_\alpha = 2T_p$. The rest of the plasma parameters and the numbers of particles per cell are given in Table 1. We compare two qualitatively different cases involving the parallel and oblique fire-hose instabilities and the ion-cyclotron and mirror instabilities. The parameters in each case are chosen to be in the observed range and to reduce the computation cost of the simulations. After the initial conditions of the simulation are set, the system is allowed to evolve freely in time.

## 3. Simulation Results

### 3.1. Uniform and Stationary Background

As discussed in the Introduction, the magnetic helicity signatures of instabilities in a nonlinear phase are not what the linear theory predicts. This conclusion is true in a 2D configuration, and we confirm it here in 3D. The relative streaming of the alpha particles with respect to the protons introduces an asymmetry into the system. According to the linear theory (Podesta & Gary 2011b), the growth rates of the nearly circularly polarized waves propagating in the direction of the streaming and in the opposite direction are unequal. From here, one may conclude that the former waves will have a larger intensity than the latter when the instability develops, producing a uniform-sign helicity.

The 2D numerical simulations have shown that this is the case at the initial stage of the instability (Markovskii et al. 2018, see their Figure 10). However, as time goes on, the positive-propagation intensity decreases more strongly at larger wavenumbers and falls below the negative-propagation intensity. The reason is that as the instability grows, the initially unstable modes may become stable and vice versa. Let us now consider the 3D run I, in which the instability is driven by the proton temperature anisotropy $T_{\perp p}/T_{\parallel p} > 1$. Figure 1 displays a normalized spectrum of the magnetic helicity $\sigma_m$ in the nonlinear phase, at $t = 340\ \Omega_p^{-1}$. We calculate $\sigma_m$ according to the formula

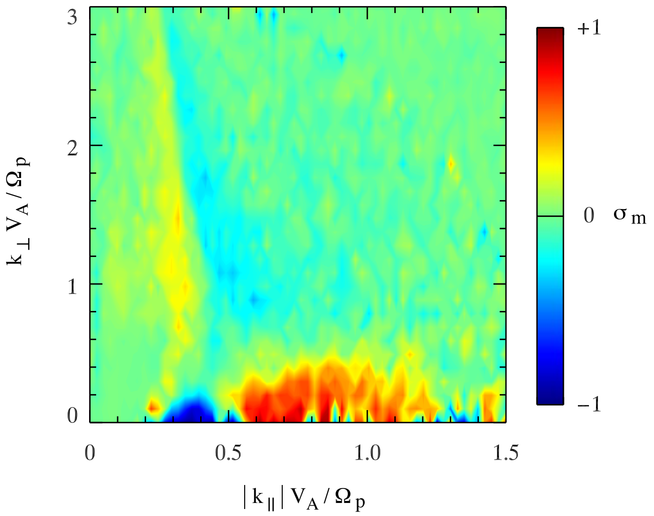

**Figure 1.** Normalized magnetic helicity spectrum $\sigma_m$ in run I at $t = 340\ \Omega_p^{-1}$.

$$\sigma_m = k\,\langle \delta \boldsymbol{A} \cdot \delta \boldsymbol{B}^* \rangle / \langle |\delta \boldsymbol{B}|^2 \rangle, \qquad (10)$$

where $\delta \boldsymbol{A}$ and $\delta \boldsymbol{B}$ are spatial Fourier transforms of the vector potential and magnetic field, the asterisk denotes a complex conjugate, and the dot denotes a dot product. Here the angle brackets indicate averaging over the azimuthal angle for each pair of wavenumber components $|k_\parallel|$ and $k_\perp = \sqrt{k_y^2 + k_z^2}$ parallel and perpendicular to the mean magnetic field $\boldsymbol{B}_0$.

As can be seen from the figure, the magnetic helicity, which is generated by nearly parallel-propagating proton-cyclotron waves, changes sign at $|k_\parallel| \approx 0.56\, \Omega_p / V_{\rm A}$. To verify that the helicity sign is consistent with the relative wave intensities, we calculate the magnetic spectrum of fluctuations propagating along the background magnetic field. For parallel propagation, the spatial Fourier transforms of the fluctuations can be separated into waves going in the positive and negative directions along the background magnetic field (Terasawa et al. 1986). The normalized fluctuation field intensity $I_0 = |\delta \boldsymbol{B}(k_\perp = 0)|^2 / B_0^2$ of these waves is shown in Figure 2 at $t = 340\ \Omega_p^{-1}$. The wavenumber of the helicity sign reversal in Figure 1 corresponds to the crossing point of the red and black lines in Figure 2. We note also that in this 3D run the signal-to-noise ratio at the crossing point is much higher than it is in the 2D run presented by Markovskii et al. (2018). This provides further evidence that the helicity sign reversal is a physically meaningful feature of the spectrum.

This configuration may be responsible for the sign reversal of the reduced magnetic helicity spectrum in the solar wind along the spacecraft sampling line. Such reversals are often observed in connection with spectral power elevations above the ambient turbulence level that are presumably associated with instabilities (Markovskii & Vasquez 2022c, see their Figure 1). To demonstrate this, we use an artificial spacecraft probe in our simulations. The reduced magnetic helicity spectrum $\tilde{\sigma}_m$, normalized to $|\delta \boldsymbol{B}|^2$, is calculated from the off-diagonal TN component of a two-point correlation function of the magnetic field in the RTN coordinate system (Matthaeus et al. 1982). The $\hat{\boldsymbol{R}}$-direction is taken along the sampling path

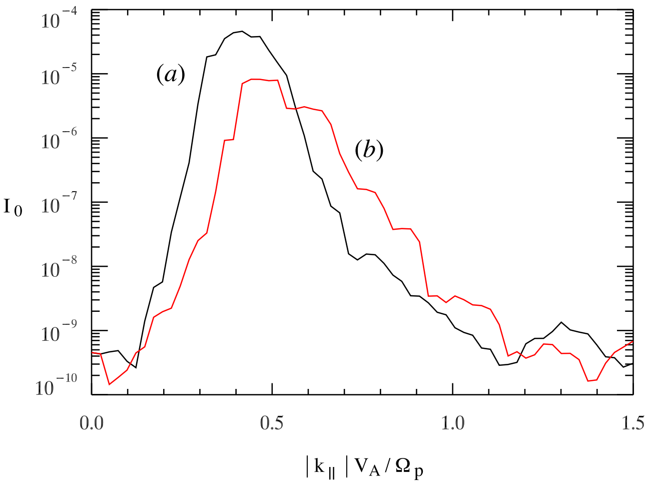

**Figure 2.** Normalized magnetic field intensity $I_0$ of the waves propagating in (a) the direction of the alpha-particle drift (black line) and (b) the opposite direction (red line) as a function of the parallel wavenumber at $t = 340\ \Omega_p^{-1}$ in run I.

of the artificial probe, which is a line perpendicular to the $z$-axis and inclined at the angle $\theta$ to the $x$-axis. The $\hat{\boldsymbol{N}}$-direction is assigned to the $z$-axis, and $\hat{\boldsymbol{T}}$ completes a right-handed coordinate system. In order to get more statistical data, we run the probe along multiple lines at different $y$. The magnetic field is sampled at a fixed time of the simulation run.

The power elevations in the solar wind are preferentially observed at small sampling angles $\theta$. Therefore, we choose $\theta = 25°$. The $\tilde{\sigma}_m$ spectrum corresponding to the full spectrum in Figure 1 is displayed in Figure 3 (black curve ($a$)). The wavenumber of the field reversal in Figure 3 is smaller than that in Figure 1 by approximately a factor of $\sin 25°$. At earlier times, when the instability is still growing, $\tilde{\sigma}_m$ is uniformly negative with no sign reversal (green curve ($b$) in Figure 3), in agreement with the full spectrum at that time (not shown).

We now turn to the case $T_{\perp p}/T_{\parallel p} < 1$, in which the temperature anisotropy excites parallel and oblique fire-hose instabilities. Again, the nonlinear evolution here invalidates the prediction of the linear theory, but in a different way. In the linear limit, only the parallel mode contributes to the magnetic helicity. However, the oblique instability saturates by nonlinear interactions and transformation to nearly parallel Alfvén modes, whereas the initial parallel modes are reabsorbed by the particles (Hellinger & Matsumoto 2001; Hellinger & Trávníček 2006). The full magnetic helicity spectrum $\sigma_m$ in the nonlinear phase is shown in Figure 4. The spectrum is "pinched" at $|k_\parallel| \approx 0.45\, \Omega_p/V_A$ and consists of two domains. A similar configuration is found in the observational data of Podesta & Gary (2011a, see their Figure 2).

The time evolution of the unstable modes is plotted in Figure 5. It is convenient to track the wave intensity at local maxima in the wavenumber space. There are two maxima present at all times in runs I and II at the parallel and oblique propagation directions. The blue curve ($a$) in Figure 5 shows how the initial parallel fire-hose mode in run II is replaced by the one resulting from the saturation of the oblique mode sometime around $t = 260\ \Omega_p^{-1}$. The oblique mode (green curve ($b$)) is reabsorbed eventually, and only the parallel one persists through the end of the simulation. This is distinct from run I, where the initial parallel-propagating proton-cyclotron mode

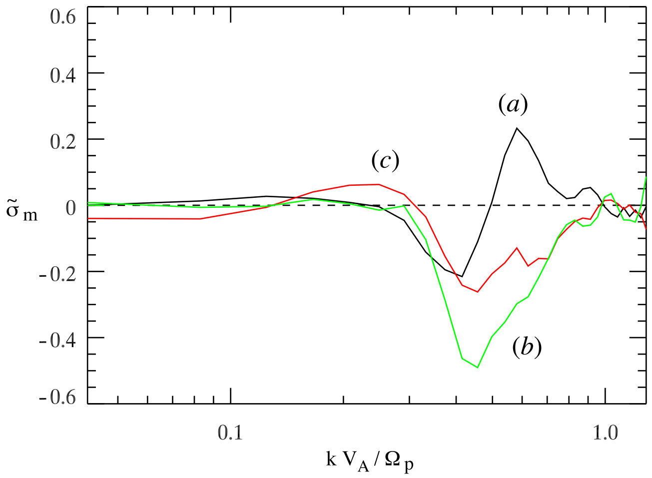

**Figure 3.** Reduced magnetic helicity spectrum $\tilde{\sigma}_m$ normalized to $|\delta \boldsymbol{B}|^2$ in run I at $t = 340\ \Omega_p^{-1}$ (black curve ($a$)), run I at $t = 250\ \Omega_p^{-1}$ (green curve ($b$)), and run III $t = 230\ \Omega_p^{-1}$ (red curve ($c$)). The plots are smoothed over two neighboring points.

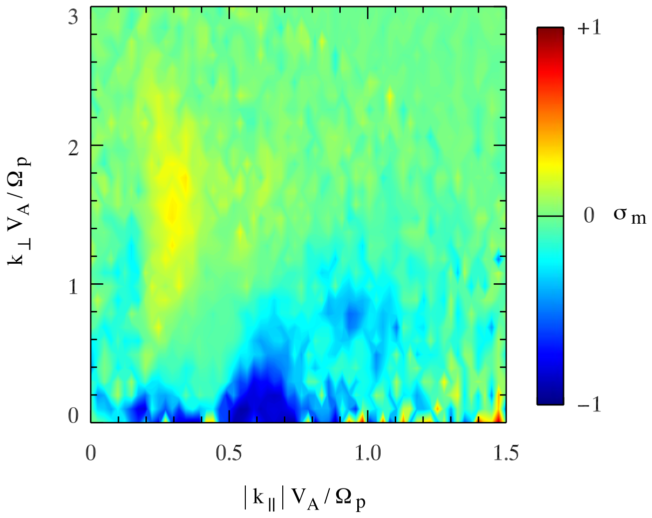

**Figure 4.** Normalized magnetic helicity spectrum $\sigma_m$ in run II at $t = 290\ \Omega_p^{-1}$.

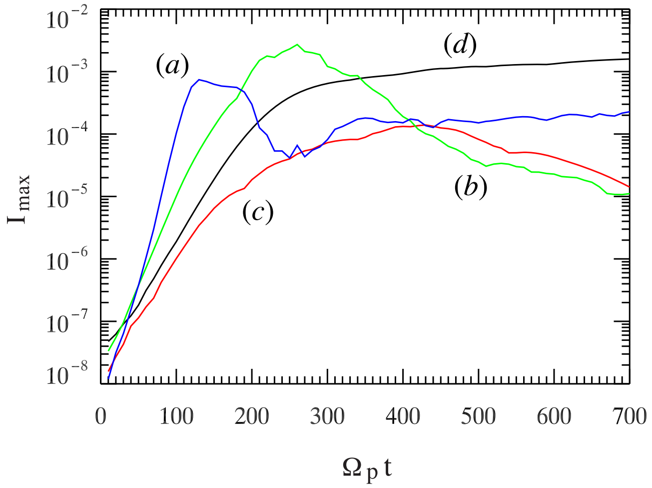

**Figure 5.** Time evolution of local-maximum intensities in the wavenumber space of the parallel fire-hose wave-mode in run II (blue curve ($a$)), the oblique fire-hose wave-mode in run II (green curve ($b$)), the proton-cyclotron mode in run I (red curve ($c$)), and the mirror mode in run I (black curve ($d$)).

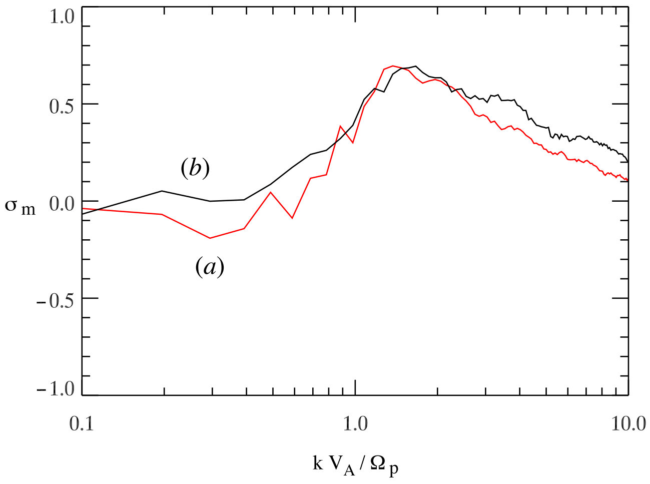

**Figure 6.** Normalized magnetic helicity spectrum $\sigma_m$ in run IV (red curve (*a*)) and run V (black curve (*b*)).

(red curve (*c*)) is reabsorbed and the oblique mirror mode (black curve (*d*)) dominates the spectrum at later times.

### 3.2. Turbulent Ambient Medium

Let us now turn to a turbulent ambient medium. Our setup here is similar to what was used by Markovskii et al. (2019). The ambient medium is introduced in the simulation as described in Section 2. The turbulence rapidly develops from the seed spectrum by spreading from lower to higher wavenumbers and then enters a quasi-steady phase where the variation of the spectrum is much slower. The resulting quasi-steady turbulence matches the observed properties of the solar wind fluctuations at 1 au, in particular, the rms amplitude at the ion kinetic scales. At larger scales, it obeys the Kolmogorov law and is weakly compressive. At smaller scales, the spectrum steepens compared to the Kolmogorov slope, and the fluctuations become more compressive.

In our present simulations, the cross-helicity of the initial seed spectrum is not zero. This introduces an imbalance into the turbulence that develops later on. The turbulence then generates a magnetic helicity signature at the ion kinetic scales, which is confined to a certain range of wavevectors. As discussed in the Introduction, this is true even if the wavevectors of the turbulent fluctuations are strictly perpendicular to the mean magnetic field $B_0$ and no linear waves propagating in the direction of $B_0$ are present in the system (Markovskii & Vasquez 2013, 2016).

To verify this in the anisotropic-temperature case, we ran 2D simulations in the *y*-*z* plane perpendicular to the background magnetic field. Since the parallel wavenumbers of the fluctuations are cut off this way, the instability is not excited and the turbulence is separated from the instability. The 2D approximation for the turbulence alone is reasonable because in the full 3D space it is anisotropic with the preferential wavevector direction perpendicular to $\boldsymbol{B}_0$. The resulting magnetic helicity spectrum of the turbulence is displayed in Figure 6. The spectrum is averaged over the polar angle for each *k* and over the time period $350\,\Omega_p^{-1} < t < 450\,\Omega_p^{-1}$ in the quasi-steady phase of the turbulence evolution. As is seen from the figure, the helicity signature is not affected strongly by the opposite senses of the temperature anisotropy as long as the total plasma betas are comparable. This spectrum is similar to the observed one in the solar wind, as can be shown, for instance, by comparing it to Figure 1 of Markovskii et al. (2015, 2016).

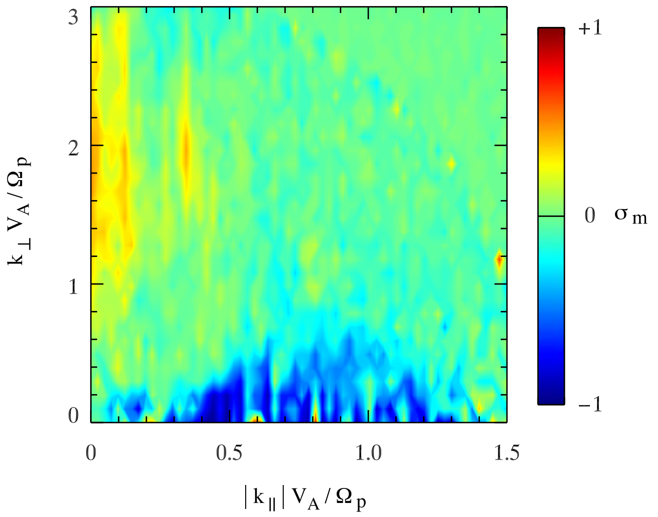

**Figure 7.** Normalized magnetic helicity spectrum $\sigma_m$ in run III at $t = 230\,\Omega_p^{-1}$.

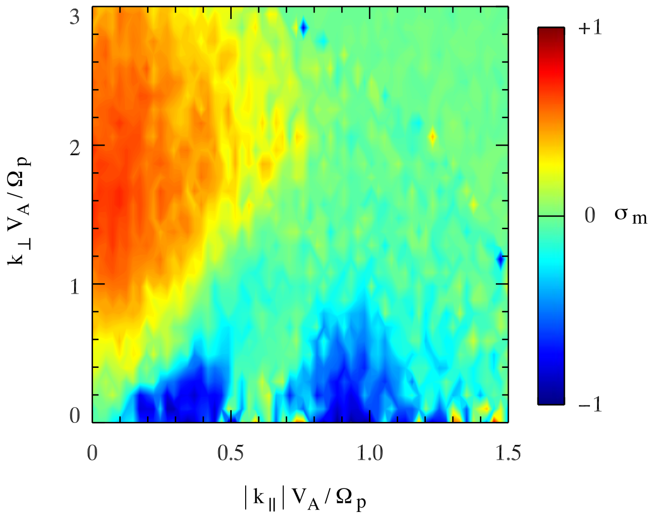

**Figure 8.** Normalized magnetic helicity spectrum $\sigma_m$ in run III at $t = 520\,\Omega_p^{-1}$.

The helicity signatures of the coexisting turbulence and instability in the full 3D space are shown in Figures 7–9 in the case $T_{\perp p}/T_{\| p} < 1$. At earlier times (Figure 7), the turbulence helicity is confined within a narrow range of the wavevector angles with respect to $\boldsymbol{B}_0$ because the turbulence was initiated in this range. In turn, the instability produces a single domain of a uniform-sign helicity. We can also calculate the reduced magnetic helicity in the same way as for the uniform-background configuration in Figure 1. Since the turbulence and instability helicities have opposite signs, this is reflected in the reduced spectrum (red curve (*c*) in Figure 3) as a sign reversal.

At later times (Figure 8), the angular range of the turbulence helicity spectrum becomes wider, 90° ± 20°. Notice that the helicity is plotted as a function of the absolute value of $k_\|$. This is in agreement with the solar wind results of Podesta & Gary (2011a), who observed a broad signature around the perpendicular propagation direction, 90° ± 30°. The instability

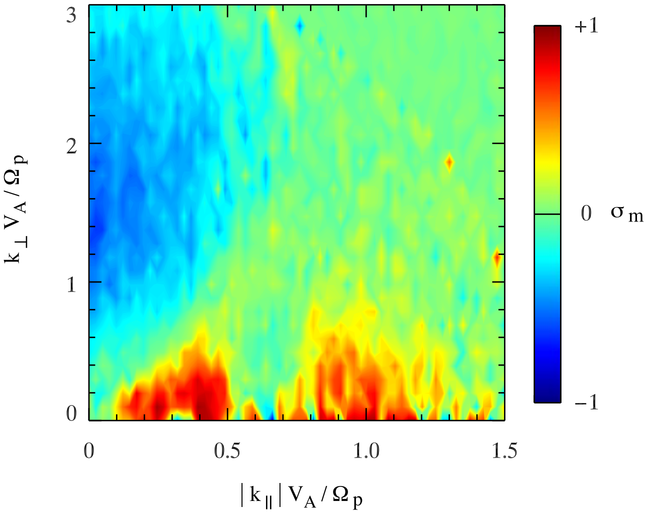

**Figure 9.** Normalized magnetic helicity spectrum $\sigma_m$ in run VI at $t = 520\ \Omega_p^{-1}$.

signature again splits in two domains, as in the uniform-background configuration, with the separation being more pronounced and resembling closer the configuration observed by Podesta & Gary (2011a) in their Figure 2. We note also that Figure 3 in Podesta & Gary (2011a) appears to show a sign reversal within the domain of the helicity associated with an instability similar to the one seen in our Figure 1.

The sign of spectral magnetic helicity signature associated with the solar wind turbulence is anticorrelated with the sign of the cross-helicity integrated over the observed interval that determines the spectrum (Hamilton et al. 2008). As shown by Smith et al. (1984), the change of the cross-helicity sign is equivalent to the change of the direction of the mean magnetic field, to or away from the Sun, assuming that the direction of propagation of the fluctuations remains the same, outward from the Sun in the present case. When the alpha-particle streaming with respect to the protons is present, the relative streaming velocity is also directed outward from the Sun regardless of the magnetic field direction.

Podesta & Gary (2011a) analyzed the magnetic helicity in the northern and southern polar regions, in which the large-scale magnetic field had opposite directions, and observed opposite signs of the helicity signatures corresponding to both turbulence and instability. Note, however, that this finding is not exclusive to the polar regions because both directions are also observed in the ecliptic plane (Goldstein et al. 1994; Leamon et al. 1998; He et al. 2011). To model these observations, we modified run III by changing the sign of $\sigma_c$ and $V_{d\,\alpha}$. The magnetic helicity in the resulting run VI is shown in Figure 9. Comparing Figures 8 and 9, one can see that, apart from the sign, the helicity structure in these runs is practically the same. In the present case, the magnetic field direction is a geometric factor that does not produce any physical effect. There are no differences in the helicity magnitude or the domains of nonzero helicity.

## 4. Conclusion

We have analyzed the spectral magnetic helicity associated with the proton temperature anisotropy instability. We used 2D and 3D hybrid numerical simulations with kinetic ions and fluid electrons, which take into account nonlinear effects of the instability. The simulations showed a more complex structure of the helicity spectrum than predicted by the linear theory. The overall helicity is determined by a relative intensity of the unstable waves propagating along the magnetic field and in the opposite direction. This relative intensity, as a function of the wavenumber, changes as the instability progresses from the linear to nonlinear phase because of the saturation.

In the case $T_{\perp p}/T_{\parallel p} > 1$, we have confirmed in the 3D setup that the helicity signature in the nonlinear phase of the proton-cyclotron instability exhibits a sign reversal, unlike the linear phase where the sign is uniform. The reason is that, in parts of the spectrum, the waves propagating in the opposite direction of the magnetic field start to dominate over time, even though their intensity was initially lower. The sign reversal in the full spectrum is consistent with that in a reduced spectrum in the solar wind along the spacecraft sampling path. It is frequently observed in connection with the magnetic power elevations presumably caused by the thermal ion instabilities. To demonstrate that, we have used an artificial spacecraft probe in our simulations and calculated the reduced spectra.

When $T_{\perp p}/T_{\parallel p} < 1$, the nonlinear effects also change the magnetic helicity produced by the fire-hose instability, but in a different way. Unlike the $T_{\perp p}/T_{\parallel p} > 1$ case, where the oblique mirror mode does not contribute to the helicity signature, the oblique fire-hose mode does. This happens at later times of the instability evolution when the oblique fire-hose mode saturates by transforming to an Alfvén mode. The instability produces two separate domains of nonzero helicity of the same sign. This structure is consistent with the observed spectrum of the magnetic helicity as a function of the angle between a local mean magnetic field and the flow direction of the solar wind.

We have also evaluated the helicity of the instabilities coexisting with an ambient turbulence, which is always the case in the solar wind. The turbulence generates its own helicity signature even when its wavevectors are confined to the plane perpendicular to the mean magnetic field. The sign of the magnetic helicity at the kinetic scales of the developed turbulence is determined by the sign of the cross-helicity at the injection scales of the seed spectrum used to initiate the turbulence. Our 3D simulations show that the magnetic helicity of the turbulence extends over a wide range of angles around the direction perpendicular to the mean magnetic field, in agreement with the observations in the solar wind. When the helicity signatures of the turbulence and instability are combined, they can have either the same or opposite signs. In the latter case, the reduced helicity spectrum also has a sign reversal consistent with the observational data in the solar wind.

## Acknowledgments

This work is supported by the NASA Heliophysics Supporting Research Program under grants 80NSSC21K1674 and 80NSSC19K0832 and by the NSF SHINE Program under grant AGS2005982 to the University of New Hampshire. The simulations were performed on Marvin, a Cray CS500 supercomputer at the University of New Hampshire. Marvin is supported by the NSF Major Research Instrumentation Program under grant AGS1919310.

## ORCID iDs

Bernard J. Vasquez https://orcid.org/0000-0001-8593-7289

## References

Bowen, T. A., Bale, S. D., Bonnell, J. W., et al. 2020a, ApJ, 899, 74

Bowen, T. A., Mallet, A., Huang, J., et al. 2020b, ApJS, 246, 66

Goldstein, M. L., Roberts, D. A., & Fitch, C. A. 1994, JGR, 99, 11519

Hamilton, K., Smith, C. W., Vasquez, B. J., & Leamon, R. J. 2008, JGRA, 113, A01106

He, J., Marsch, E., Tu, C., Yao, S., & Tian, H. 2011, ApJ, 731, 85

He, J., Tu, C., Marsch, E., & Yao, S. 2012, ApJL, 745, L8

He, J., Wang, L., Tu, C., Marsch, E., & Zong, Q. 2015, ApJL, 800, L31

Hellinger, P., & Matsumoto, H. 2001, JGR, 106, 13215

Hellinger, P., & Trávníček, P. 2006, JGRA, 111, A01107

Huang, S. Y., Zhang, J., Sahraoui, F., et al. 2020, ApJL, 897, L3

Leamon, R. J., Smith, C. W., Ness, N. F., Matthaeus, W. H., & Wong, H. K. 1998, JGR, 103, 4775

Markovskii, S. A., Chandran, B. D. G., & Vasquez, B. J. 2018, ApJ, 856, 153

Markovskii, S. A., & Vasquez, B. J. 2013, ApJ, 768, 62

Markovskii, S. A., & Vasquez, B. J. 2016, ApJ, 820, 15

Markovskii, S. A., & Vasquez, B. J. 2022a, ApJ, 924, 111

Markovskii, S. A., & Vasquez, B. J. 2022b, ApJ, 930, 120

Markovskii, S. A., & Vasquez, B. J. 2022c, ApJ, 941, 72

Markovskii, S. A., Vasquez, B. J., & Chandran, B. D. G. 2019, ApJ, 875, 125

Markovskii, S. A., Vasquez, B. J., & Chandran, B. D. G. 2020, ApJ, 889, 7

Markovskii, S. A., Vasquez, B. J., & Smith, C. W. 2015, ApJ, 806, 78

Markovskii, S. A., Vasquez, B. J., & Smith, C. W. 2016, ApJ, 833, 212

Matthaeus, W. H., Goldstein, M. L., & Smith, C. W. 1982, PhRvL, 48, 1256

Podesta, J. J., & Gary, S. P. 2011a, ApJ, 734, 15

Podesta, J. J., & Gary, S. P. 2011b, ApJ, 742, 41

Smith, C. W., Goldstein, M. L., Matthaeus, W. H., & Viñas, A. F. 1984, JGR, 89, 9159

Terasawa, T., Hoshino, M., Sakai, J.-I., & Hada, T. 1986, JGR, 91, 4171

Vasquez, B. J. 1995, JGR, 100, 1779

Vasquez, B. J. 2015, ApJ, 806, 33

Zhao, G. Q., Lin, Y., Wang, X. Y., et al. 2021, ApJ, 906, 123